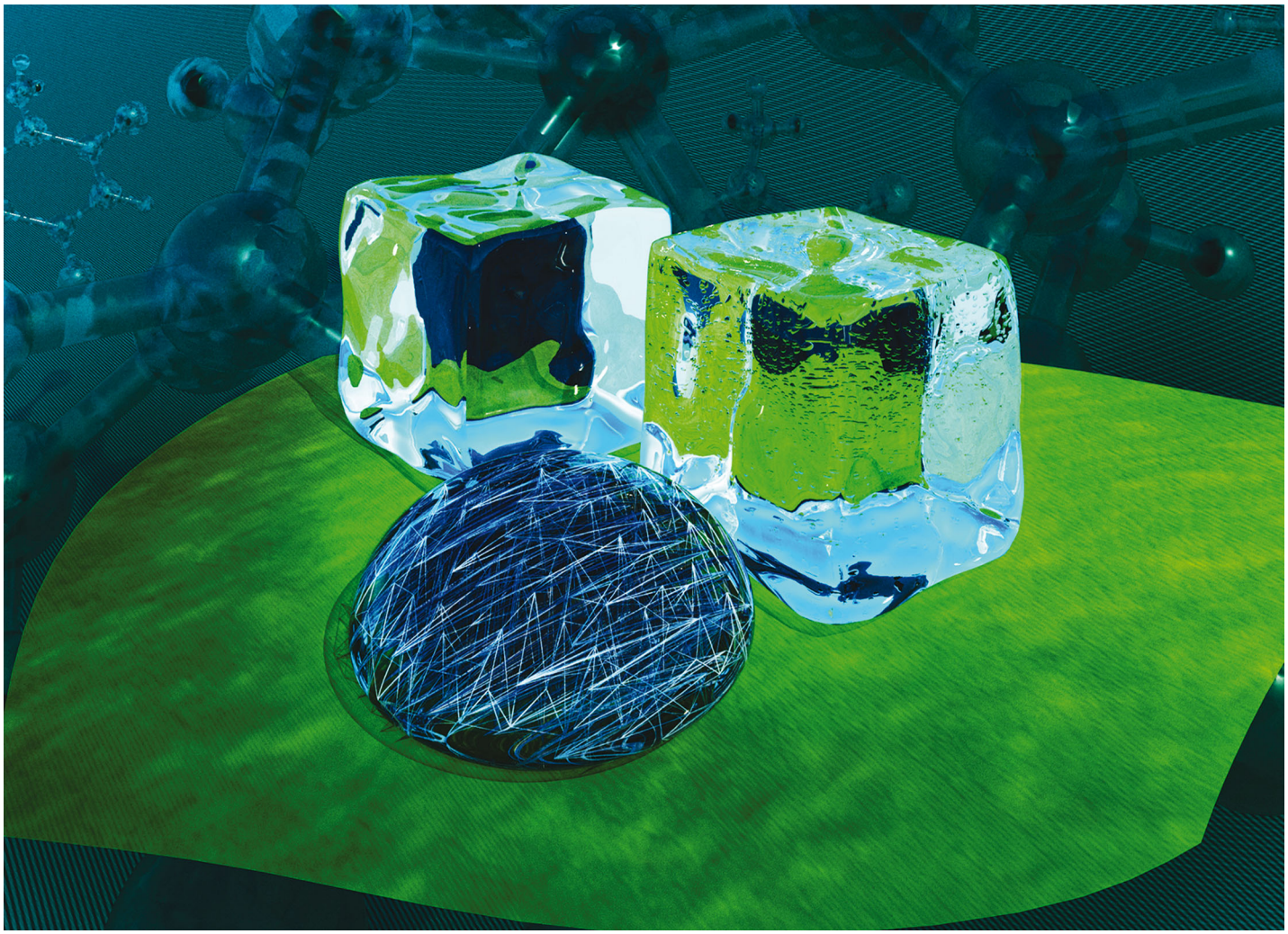

Highlighting research performed in the Complex Fluid Lab of Prof. Chi-Chung Hua from the Department of Chemical Engineering, National Chung Cheng University, Taiwan.

PBTTT-C_{16} sol–gel transition by rod associations and networking

Yi and Hua report an unconventional way by which the molecular weight of a conjugated polymer can impact its solution, sol, gel and thin film properties, all beginning with a subtle difference in the supramolecular aggregate conformation fostered in pristine solutions.

As featured in:

See Han-Liou Yi and Chi-Chung Hua, *Soft Matter*, 2019, **15**, 8022.

ROYAL SOCIETY OF CHEMISTRY | Celebrating IYPT 2019

rsc.li/soft-matter-journal

Registered charity number: 207890

Published on 12 September 2019. Downloaded by National Synchrotron Radiation Research on 1/9/2020 4:42:14 AM.

Soft Matter

PAPER

View Article Online
View Journal | View Issue

Check for updates

Cite this: *Soft Matter*, 2019, **15**, 8022

PBTTT-C_{16} sol–gel transition by rod associations and networking†

Han-Liou Yi and Chi-Chung Hua *

A low-molecular-weight poly(2,5-bis(3-hexadecylthiophen-2-yl)thieno[3,2-*b*]thiophene) (designated as Lw-pBTTT-C_{16}) in a fair solvent (chlorobenzene, CB) displays peculiar structural, mechanical, and electronic features during sol–gel transition. Using comprehensive (multiscale) dynamic/static analysis schemes, the Lw-pBTTT-C_{16}/CB solution (10 mg mL^{-1}) is shown to capitalize on rod associations and networking to form a gel, in stark contrast with its high-molecular-weight companion previously reported to form gels through hierarchical colloidal bridging. The present study reveals, however, that the molecular weight of pBTTT-C_{16} has a subtle impact on the gelation behaviors through the rarely recognized, contrasting supramolecular conformations (rod-like *vs.* wormlike) of the aggregate clusters fostered in the pristine solution. The ac conductivity nearly doubles as a result of improved (mesoscale) packing of cylindrical aggregates near the gel state as well as enhanced backbone rigidity of the constituting chains. Other distinguishing features include: (1) there is no real crossover of the dynamic moduli (G' and G'') upon increasing the temperature from gel (T = 15 °C) to solution (T = 80 °C) states. (2) The gel is about a hundredfold softer in dynamic modulus, yet more resilient with a fivefold increase in the yield strain. Both viscoelastic features are expected to greatly benefit the gel processability. (3) The coexistent microgels and cylinder (aggregate) bundles form a peculiar gel network that has not been reported previously with polymer or colloidal gels. The overall findings provide new mechanistic insight into the phenomenological effects of molecular weight for the pBTTT-C_n series in solution, sol, gel, and thin film.

Received 7th July 2019,
Accepted 12th September 2019

DOI: 10.1039/c9sm01362h

rsc.li/soft-matter-journal

1. Introduction

Conjugated polymers have attracted much attention recently in organic optics/electronics technologies[1–3] for applications of organic photovoltaics (OPVs),[4,5] organic photodiodes (OPDs),[6] organic light-emitting diodes (OLEDs),[7] organic thin-film transistors (OTFTs),[8] organic electrochemical transistors (OECTs),[9] and memory devices.[10] The primary advantages consist of their excellent room-temperature and large-area solution processability, wherein the device performance may be fine-tuned through a number of variables such as polymer molecular weight,[11–14] side-chain length[15,16] and architecture,[3] the polymer concentration and solvent medium used,[17–23] in addition to the conditions (*e.g.*, thermal/flow history)[21,24–27] during sample preparation and processing. Meanwhile, this variety of molecular and experimental factors has posed notable challenges to gain precise and optimal control over the morphological/structural features in solution and thin film that are known to have a direct impact on the device performance. Clearly, future advances in this area will be largely defined by how sufficient scientific understanding is to bridge technological innovations.

Beyond solution-based processing techniques, the corresponding gel-based ones have recently emerged as a promising alternative for fabricating high-performance thin films and devices, owing to the unique three-dimensional (3-D) structural order that is especially advantageous for charge/heat transport in addition to improved mechanical strength.[19,28–53] Prior studies have revealed, however, widely diverse sol–gel transition mechanisms and microstructures for commonly studied conjugated polymers including poly(3-alkyl-thiophenes) (P3ATs),[29,30,32,33,35,36,39] poly(9,9-dialkyl fluorenes) (PFs),[34,40–44,54–56] poly(vinylene phenylenes) (PVPs),[19,45,46] and poly(2,5-bis(3-alkylthiophen-2-yl)thieno-[3,2-*b*]thiophenes) (pBTTTs).[50] It seems essential, therefore, to acquire a comprehensive understanding of the relationship between molecular attributes and microstructures when gels are used for the end applications.

The present work is aimed at resolving several enigmatic features associated with a versatile series of conjugated polymers, pBTTT-C_n, that have demonstrated high charge-carrier mobility[27,57–60] and good oxidative stability[57] in recent applications with OPVs[61,62] and OTFTs.[63] Early investigations[50,64] indicated that pBTTT-C_{16} is the only species of its kind known to exhibit a sol–gel transition under

Department of Chemical Engineering, National Chung Cheng University, Chiayi 62102, Taiwan. E-mail: chmcch@ccu.edu.tw

† Electronic supplementary information (ESI) available. See DOI: 10.1039/c9sm01362h

This journal is © The Royal Society of Chemistry 2019

Published on 12 September 2019. Downloaded by National Synchrotron Radiation Research on 1/9/2020 4:42:14 AM.

typical experimental conditions. Specifically, a pBTTT-C_{16}/chlorobenzene (CB) solution (10 mg mL^{-1}) was recently shown to form gels of varied porosities and mechanical strengths by hierarchical bridging of spherical colloids.[50] Using multiscale dynamic/structural analysis schemes, we report herein that when a similar polymer species yet with a slightly lower apparent molecular weight (*i.e.*, M_w = 51 472 *vs.* 61 309 g $mole^{-1}$, designated respectively as Lw-pBTTT-C_{16} and Hw-pBTTT-C_{16}) is utilized, the sol–gel transition mechanism and structural/material properties differ substantially under identical experimental conditions. The present study reveals, however, that the molecular weight of pBTTT-C_{16} has a subtle impact on the gelation behaviors through the rarely recognized, contrasting supramolecular conformations (rod-like *vs.* wormlike) of the aggregate clusters fostered in the pristine solution (T = 80 °C), which consequently morph into distinct packing units (cylindrical *vs.* spherical) upon reaching the sol state at the gelation temperature (T = 15 °C). The above features provide new insight into the previous findings that varying the molecular weight of pBTTT-C_n can have a significant impact on their thin-film and device properties.[11–14]

2. Experimental methods

2.1 Materials and sample preparation

The Lw-pBTTT-C_{16} sample, with an average molecular weight of M_w = 51 472 g $mole^{-1}$, was purchased from Luminescence Technology Corp. (Taiwan) and used without further purification. The solvent used to dissolve Lw-pBTTT-C_{16}, chlorobenzene (CB; Sigma-Aldrich, ≥99.5% in purity), was filtered through a 0.22 μm PVDF filter (Millipore Millex-GN) to remove dust. The benchmark 10 mg mL^{-1} Lw-pBTTT-C_{16}/CB solution was prepared with the filtered solvent. To fully dissolve the polymer in CB, the sample solution was mildly sonicated for 12 h at 80 °C,[50,64,65] whereby a transparent and homogeneous solution was obtained that is especially important for the light scattering experiments in this study. Measurements of the solution viscosity indicated no appreciable chain degradation after the sonication treatment. For comparison, we noticed that the original (inhomogeneous) solution without sonication can expedite the full gelation process, possibly through an enhanced local clustering of aggregate species. The Lw-pBTTT-C_{16}/CB solution so prepared may be brought to gel *via* short-term aging (within one day) at a low temperature (15 °C; see photographs in Fig. S1b, ESI†), and the gel structure may be largely disintegrated by heating back to 80 °C. The freshly prepared, heated solution was allowed to equilibrate for at least 2 h at 80 °C to minimize the effect of the prior sonication, and then quickly transferred to the sample carriers for all subsequent measurements. Unless stated otherwise, most measurements described below were conducted during a fast quenching from 80 °C to the gelation temperature (15 °C), when the sample was allowed to stand still for 30 min prior to the measurements. Upon reaching the gelation temperature, the effects of aging time were closely monitored until the gel network ripened in about one day. All comparisons made with a higher-molecular-weight sample, Hw-pBTTT-C_{16}/CB (M_w = 61 309 g $mole^{-1}$), were based on identical sample preparation and characterization schemes, and thus the differences in sol and gel properties between the two pBTTT-C_{16}/CB samples can be attributed to the different partition of shorter chains; see the gel permeation chromatography (GPC) data in Fig. S1c, ESI.†

2.2 Light scattering (SLS/DLS/DDLS) analyses

Light scattering (LS) measurements were performed on a laboratory-built apparatus as described elsewhere.[45,66] A 20 mW polarized diode laser (λ_0 = 785 nm; Omicron, LuxX® 785, Germany) was used as the incident light to avoid absorption by Lw-pBTTT-C_{16}/CB in the visible-light region, especially at a concentration as high as 10 mg mL^{-1}. A UV-vis spectrometer was utilized to confirm that Lw-pBTTT-C_{16}/CB shows negligible absorption at the incident light wavelength, as described in Section S1, ESI.† Besides, nearly identical absorption spectra can be noted between Lw-pBTTT-C_{16}/CB and Hw-pBTTT-C_{16}/CB,[50] suggesting that they are of the same species. The effect of incident light intensity has also been scrutinized, ensuring that the data reported were unaffected by light absorption and the consequent thermal-induced flow convection, as described in Section S2, ESI.† According to the last requirement, the laser power was attenuated to about 1 mW for the present light-scattering experiments. Moreover, ergodicity of the Lw-pBTTT-C_{16}/CB gel was assessed using a partial-heterodyne method described in Section S3, ESI.† Detailed introductions of the static, dynamic, and depolarized dynamic light scattering (SLS/DLS/DDLS) analysis schemes employed herein can be found in prior work.[50,65]

2.3 Small-/wide-angle light/X-ray scattering (SALS/SAXS/WAXS/GIWAXS) analyses

The apparatus for small-angle light scattering (SALS) measurements was described elsewhere.[45] A 2 mW He–Ne laser with a wavelength of λ_0 (=632.8 nm) was used as the incident light, and data were collected in a range of scattering angle θ = 0.7–20°. Small-angle X-ray scattering (SAXS), wide-angle X-ray scattering (WAXS), and grazing-incident wide-angle X-ray scattering (GIWAXS) measurements were carried out at beamline station BL23A of the National Synchrotron Radiation Research Center (NSRRC) in Taiwan. The scattering X-ray for the SAXS measurements covers a q-range of 0.04–3.0 nm^{-1}, with a 15 keV incident beam (wavelength λ_0 = 0.827 Å) and sample-to-detector distance of 4714 mm; the sample cell bears a thickness of 1.2 mm.

2.4 Dynamic modulus analysis

A TA Instruments DHR-2 stress-controlled rheometer was used with a cone-plate geometry (diameter = 40 mm, cone angle = 2°, and gap distance = 55 μm) and, for the time-sweep experiment on the sol–gel transition, with an aluminum double-gap cylinder geometry (the inner cup bears a diameter of 30.2 mm, the inner and outer rotor diameters are 31.97 and 34.98 mm, respectively, and both gaps bear the same size of 0.95 mm). The above geometries were equipped with a Peltier temperature controller, which maintains the system temperature at 80 °C upon loading the fresh solution sample. To minimize the effect of solvent evaporation, a solvent trap was utilized during the entire measuring process.

Published on 12 September 2019. Downloaded by National Synchrotron Radiation Research on 1/9/2020 4:42:14 AM.

Additionally, the data reported herein were confirmed to be free of the effect of solvent evaporation by closely monitoring the amount of solvent within the reservoir (for double-gap fixture) after each measurement, as well as by ensuring the absence of any abnormal and systematic rise of dynamic moduli during the strain and frequency sweeps (for both fixtures).

2.5 Optical/electron microscopy (OM/EM) analyses

Optical microscopy (OM) images were taken using a conventional microscope (Olympus BX51, Japan) equipped with a high-resolution digital camera (Olympus DP22, Japan) and a laboratory-built heating/cooling temperature controller. The samples for OM characterization were prepared by casting the Lw-pBTTT-C_{16}/CB solution into a cell having a gap size of 2 mm, followed by cooling to the gelation temperature. The scanning electron microscopy (SEM) images were taken using a scanning transmission electron microscope (Hitachi S4800-I) at an acceleration voltage of 15 kV.

2.6 Ac conductivity analysis

Measurements of ac conductivity were performed using a Solartron 1296 dielectric interface coupled to a Solartron 1260 frequency response analyzer, operated at a frequency of 2 kHz and a small voltage (200 mV) in the linear impedance region. The sample was placed between parallel-plate electrodes (diameter = 25 mm and gap size = 0.2 mm) made of stainless steel and electrically insulated with machining ceramics, along with a laboratory-built temperature controller that achieved a heating rate of 4 °C min^{-1}.

3. Results and discussion

3.1 General features of Lw-pBTTT-C_{16} sol and gel

We begin with a comparison between two different pBTTT-C_{16}/CB samples in Fig. 1, which shows the ac conductivities of the gel-to-solution samples upon steady heating (4 °C min^{-1}) along with the SEM thin-film morphologies of the gels. While the thin film produced by Hw-pBTTT-C_{16}/CB was previously shown to be composed of (spherical) micrometer-sized clusters,[50] its Lw-pBTTT-C_{16} companion is clearly characterized by the agglomeration of small fibers. The cross-sectional SEM images presented in Fig. S6, ESI† further reveal a film thickness of about 1.7 μm for the gel sample and 400 nm for the drop-cast thin film discussed in a later subsection. Both samples exhibit a notable increase in ac conductivity near the gel state, and Lw-pBTTT-C_{16}/CB nearly doubles the value achieved by Hw-pBTTT-C_{16}/CB at room temperature. These results provide unambiguous evidence showing how the (molecular-weight-dependent) microstructures of a gel material impact its electronic properties.

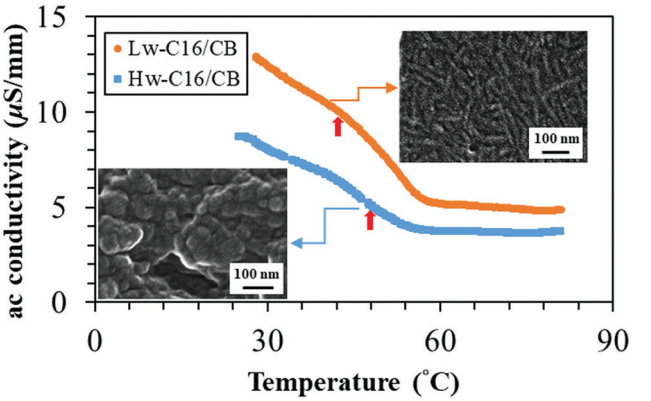

Fig. 1 Ac conductivity upon steady heating of the 10 mg mL^{-1} Lw-pBTTT-C_{16}/CB gel (orange spheres) incubated for 24 h at 15 °C, as compared with the result for the Hw-pBTTT-C_{16}/CB gel (blue squares)[50] under similar experimental conditions. SEM thin-film morphologies taken from the gel samples at T = 15 °C are also shown. The red arrows indicate the gelation temperatures inferred from dynamic modulus/light scattering analyses for the two pBTTT-C_{16} samples.

Without access to temperatures below the ambient one for the facility presently used, we expect that the disparity in ac conductivity for the gel state at 15 °C should be even more prominent, as previously demonstrated for the P3HT gels.[29,30,32] Consistent with the present observations, prior work indicated that the thin films fabricated from pBTTT-C_n of varying molecular weight can substantially alter their electronic properties.[11–14] The present analyses reveal, however, that the molecular weight of pBTTT-C_{16} has a subtle impact on the gelation behaviors through the contrasting supramolecular conformations of the aggregate clusters fostered in the pristine solution, as discussed in detail below.

We first summarize the essential DLS/DDLS and SAXS features for the (fresh) pBTTT-C_{16}/CB solutions at 80 °C, which are very important to understand the corresponding sol properties at a lower temperature. Despite the disparities seen in Fig. 1, the results shown in Fig. S7 and Table S1, ESI† reveal little difference in the DLS/DDLS characterization of their solutions at 80 °C. The DDLS features, in particular, indicate that in both cases the aggregate clusters are notably anisotropic in shape. In contrast, Fig. S8, ESI† reveals distinct SAXS profiles for the two solutions. Although the high-q feature ($q > 1$ nm^{-1}), $I(q) \sim q^{-1}$, indicates a similar rod-like attribute of the building (smaller) aggregates, the intermediate-q profile ($0.2 < q < 1$ nm^{-1}) displays distinct features of $I(q) \sim q^{-2.1}$ and $I(q) \sim q^{-1.1}$ for the Hw- and Lw-pBTTT-C_{16}/CB solutions, respectively. Clearly, the aggregates differ in their detailed structures in the two solutions, and the (mesoscale) cylindrical aggregate formed by Lw-pBTTT-C_{16} (see also later discussions) appears to be much more persistent in supramolecular rigidity. As the solution is first brought into the sol state at the gelation temperature (15 °C), the DDLS analysis shown in Fig. S9, ESI† reveals that Lw-pBTTT-C_{16}/CB retains its anisotropic feature, whereas Hw-pBTTT-C_{16}/CB was previously shown to turn into spherical aggregates immediately, which, in turn, triggered a series of hierarchical colloidal bridging steps to form gels.[50]

In summary, combined DLS/DDLS/SAXS analyses on the solution and sol of the two representative pBTTT-C_{16} samples clearly reveal that even a slight difference in the apparent molecular weight can have a profound impact on the supramolecular aggregate properties in solution that, in turn, lead to strikingly distinct gelation behaviors, as systematically revealed

 This journal is © The Royal Society of Chemistry 2019

Published on 12 September 2019. Downloaded by National Synchrotron Radiation Research on 1/9/2020 4:42:14 AM.

in the following analyses. While the Lw-pBTTT-C_{16}/CB solution fosters rigid cylindrical aggregates, possibly due to the dominant population of shorter chains in Fig. S1c, ESI† that bear a higher chain rigidity, the Hw-pBTTT-C_{16}/CB solution produces similar aggregate species that are wormlike in nature. This explains why the aggregate species later morphed into distinctively different colloidal particles (cylindrical *vs.* spherical) upon reaching the sol state at a lower temperature. Interestingly, these findings should point to an additional consideration in interpreting the effects of polymer molecular weight for applications with a conjugated polymer solution, gel, and even thin film.

3.2 Identification of the gel points

In prior work on the Hw-pBTTT-C_{16}/CB sol–gel transition, we showed that the gel points may be unambiguously identified by combined rheological and light-scattering characterization.[50] For a similar purpose, the Lw-pBTTT-C_{16}/CB gel incubated at 15 °C was left undisturbed for 24 h before a steady heating was carried out. Fig. 2 presents the dynamic modulus responses, where the result for Hw-pBTTT-C_{16}/CB is also included for comparison. The general feature for Hw-pBTTT-C_{16}/CB is typical of a polymer gel–sol transition in that the material behaves in a solid-like manner at low temperatures with $G' > G''$ and then becomes liquid-like at high temperatures with $G' < G''$; the crossover point, $G' = G''$, is often referred to as the gelation temperature, T_{Gel}. The results for Lw-pBTTT-C_{16}/CB differ substantially, however. First of all, there is no real "crossover" point (see the inset figure of Fig. 2a) of the two dynamic moduli during the gel–sol transition; in this case, the "gel" point at $T \sim 40$ °C is identified where the two moduli are closest to each other. Similar features (*i.e.*, no crossover point) have been reported for the gels formed by hydrogenated castor oil (HCO)[67] and polyamide fibrous colloids.[68] Moreover, a plateau of G', which lies substantially above G'', can be clearly observed in the high-temperature region up to $T \sim 80$ °C, suggesting that certain gel microstructures persist[67] during the gel–sol transition, which takes about 20 min in the temperature sweep. (It will be shown in Fig. 6, however, that the usual trend $G'' > G'$ applies at the same strain and frequency if the system begins with the sol state that contains no residual gel microstructures.)

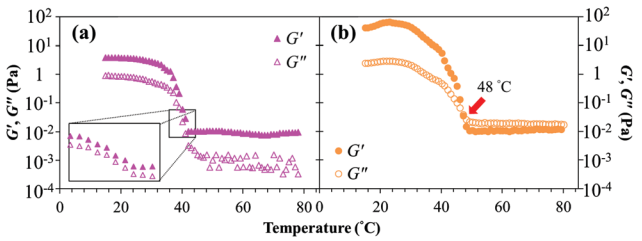

Fig. 2 Dynamic modulus responses (strain = 0.01 and frequency = 10 rad s^{-1}) upon steady heating the (a) Lw-pBTTT-C_{16}/CB and (b) Hw-pBTTT-C_{16}/CB gels that have been incubated for 24 h at 15 °C. The gelation temperature (T_{Gel}) is often defined as the crossover of the storage (G') and loss (G'') moduli, as indicated by the arrow in (b) for the Hw-pBTTT-C_{16}/CB gel. The inset, magnified figure in (a) indicates that there is no real crossover of the two dynamic moduli.

The corresponding mechanical strength remains moderately low, however, as reflected in a considerably lower value of dynamic modulus in the comparison shown in Fig. 2.

Fig. 3 shows the corresponding DLS responses for Lw-pBTTT-C_{16}/CB as investigated in Fig. 2, and the inset figure shows the average scattering intensity as a function of system temperature. In contrast with the (four-stage) complex evolution of the scattering intensity previously reported for the Hw-pBTTT-C_{16}/CB gel–sol transition, Lw-pBTTT-C_{16}/CB demonstrates a relatively monotonous (two-stage) evolution in the scattering intensity (see the inset figure). The transition point identified at 42 °C is in close agreement with the dynamic modulus response discussed with Fig. 2a. Interestingly, the gelation temperature inferred by the two analysis schemes above appears to approximately match the inflection point in the ac conductivity curve in Fig. 1, where the growth of electron conductivity starts to exhibit a slow-down with further temperature reduction. Alternatively, the variable range hopping (VRH) model[69,70] that accounts for hopping conductivity in disordered systems was used to examine the temperature dependence of the ac conductivity during the gel–sol transition. Although the behavior of ac conductivity noticed in Fig. 1 differs fundamentally from those typically observed for systems whose electron conductivity is governed by the hopping mechanism[71–75] (*i.e.*, the conductivity increases with increasing system temperature, as opposed to the present observation for pBTTT-C_{16} that undergoes a gel–sol transition), the gelation temperature (41 °C) inferred from the analysis shown in Fig. S11, ESI† is in close agreement with the results noted above.

Turning to the main figure in Fig. 3, we note that there are three relaxation modes, as indicated on the right panel. Beginning from the gel state, it should be clear that the mode properties remain basically unchanged up to $T = 50$ °C, which is close to the gel point. Passing the gel point, a systematic shift of all three relaxation modes toward shorter decay times can be observed. The above static and dynamic features suggest that the bulk network of rod associations (see later discussion) that form near the gel point remains largely unaltered at temperatures below the gel point.

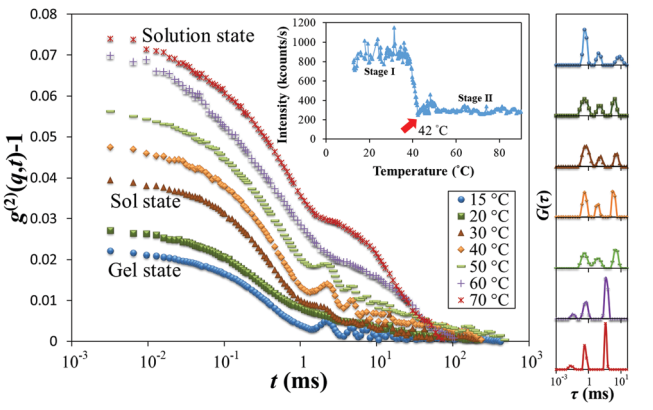

Fig. 3 Temperature dependence of the intensity correlation function (ICF), $g^{(2)}(q,t) - 1$, and the associated decay time distribution (right panels) for Lw-pBTTT-C_{16}/CB that begins with the gel state at 15 °C, followed by a steady heating (4 °C min^{-1}). The inset figure shows the corresponding average scattering intensity at $\theta = 90°$ during the same heating process.

Published on 12 September 2019. Downloaded by National Synchrotron Radiation Research on 1/9/2020 4:42:14 AM.

Meanwhile, a similar wavy feature at long decay times for the gelling sample has been observed for the Hw-pBTTT-C_{16}/CB gel–sol transition.[50]

In summary, the Lw-pBTTT-C_{16}/CB gel–sol transition is seen to evolve in a distinct and relatively monotonous fashion when compared with its Hw-pBTTT-C_{16}/CB companion, and the disparity seems to echo the contrasting features observed in Fig. 2 for the dynamic modulus responses. Evidently, the gel network formed by cylindrical aggregates in Lw-pBTTT-C_{16}/CB is more persistent than that formed by spherical ones in Hw-pBTTT-C_{16}/CB during the gel–sol transition. In Section S4, ESI,† we supplement some detailed analyses of the DLS and DDLS data during the usual sol–gel transition, in an effort to resolve the attributes of fundamental packing units for the polymer sol and gel. While the first and second relaxation modes are identified to represent the rod-like gelator ($L \sim 15.8$ nm and $d \sim 4.5$ nm) and cylindrical aggregate ($L \sim 160$ nm and $d \sim 30$ nm), respectively, the third mode has been inferred from the later (static) scattering analysis to represent microgel particles formed by the cylindrical aggregates. Accordingly, it is possible to proceed with an unambiguous analysis of combined static scattering data that allows for a further determination of the detailed structural features during the Lw-pBTTT-C_{16}/CB sol–gel transition.

3.3 SALS/SLS/SAXS analyses of structural features of Lw-pBTTT-C_{16}/CB sol and gel

The combined scattering intensity profile, $I(q)$, for the Lw-pBTTT-C_{16}/CB sol and gel at $T = 15$ °C from SALS, SLS, and SAXS measurements allows for structural analysis over approximately four orders of magnitude in length scale. The SALS and SLS profiles are smoothly transited to the (absolute) SAXS profile through a vertical shift, with the resulting profiles presented in Fig. 4. A salient feature is that while the overall intensity profile for the initial sol state ($t = 0$ h), see Fig. 4a, consists of a low-q (SALS) and high-q (SAXS) plateau along with a long mass-fractal region in between, the eventual gel state ($t = 24$ h), see Fig. 4b, can be seen to embody two pronounced transition maxima that were previously unobserved with the Hw-pBTTT-C_{16}/CB sol–gel transition[50] in particular and other polymer gels in general.

The SALS profile at low q for the Lw-pBTTT-C_{16}/CB sol permits a precise estimate of the mean radius of gyration of the aggregate cluster—or, for convenience, microgel—using the Guinier function (the 1st term in eqn (S1) and Section S5, ESI†) to be $R_g \sim 1$ μm. Interestingly, the DLS analysis (see Fig. S10, ESI†) reveals the relaxation behavior of $\langle \Gamma \rangle \sim q^{0\sim1}$ for this microgel species, suggesting that the microsized particles formed in the sol state are relatively unstable, as sometimes observed for polymer clusters of a similar size.[50,76]

At still higher q extending to the SLS region, the intensity profile, $I(q) \sim q^{-2}$, characterizes the mass-fractal structure of the microgel interior as well as the surrounding (randomly-packed) cylinder network. To capture the mesh-like structure in either case, the formulation proposed by Shibayama *et al.*[77,78] that accounts for closely-packed, uncorrelated domains of size ξ and a mass-fractal dimension d_f is utilized (the 2nd term in eqn (S1) and Section S5, ESI†). The model fits of the combined $I_{SALS+SLS}(q)$ profile are shown by the dotted line in Fig. 4a, with the fitted parameters gathered in Table 1.

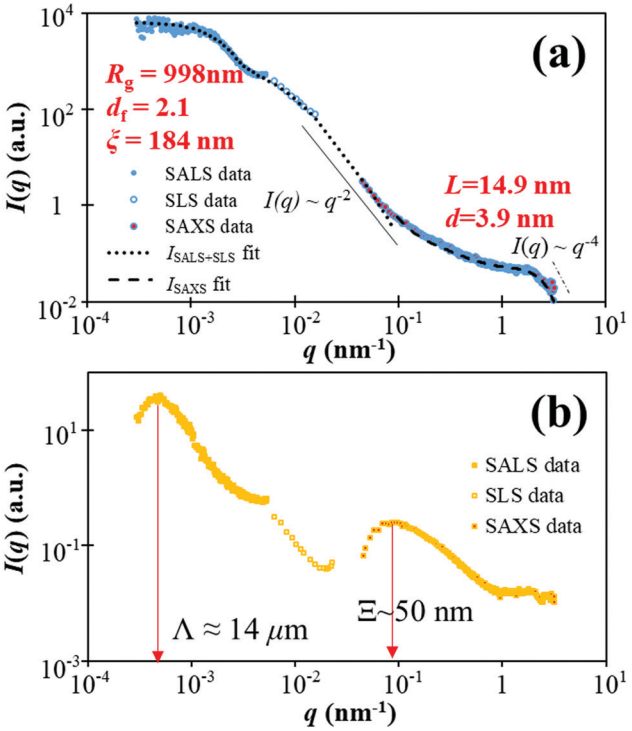

Fig. 4 Combined SALS, SLS, and SAXS intensity profiles for the Lw-pBTTT-C_{16}/CB (a) sol ($T = 15$ °C, and $t = 0$ h) and (b) gel ($T = 15$ °C, and $t = 24$ h). Note, in particular, the appearance of two major peaks at $q \sim 4 \times 10^{-4}$ and 0.1 nm^{-1} for the gel. For the sol sample, $I_{SALS}(q) + I_{SLS}(q)$ data along with the low-q part of $I_{SAXS}(q)$ ($q < 0.1$ nm^{-1}) are described by eqn (S1) (dotted line), ESI.† The remaining part of the $I_{SAXS}(q)$ data ($q > 0.1$ nm^{-1}) is fitted using eqn (S3) (dashed line), ESI.†

Meanwhile, it is of interest to note that for the gel sample shown in Fig. 4b, a pronounced peak near $q_{max} = 4.5 \times 10^{-4}$ nm^{-1} emerges, which corresponds to a characteristic length $\Lambda = 2\pi/q_{max} \approx 14$ μm. According to an OM image presented in Fig. 5, Λ here should represent the correlation length for regions of distinct two-phase structures (*i.e.*, polymer-rich or polymer-depleted)—the so-called spatial inhomogeneity length in early studies. Clearly, the distinct two-phase regions emerge at a later stage of gelation as the microgels and the surrounding cylinder bundles further coalesce.

For the SAXS profile of the sol state at still higher q, a transition from $I(q) \sim q^{-2}$ to $I(q) \sim q^{-1}$ (approximately in the range of 0.1 nm^{-1} $< q <$ 1 nm^{-1}) can be noted prior to a second plateau region. The crossover at $q_c \sim 0.15$ nm^{-1} corresponds to a correlation length or mesh size ($\xi = 2\pi/q_c$) of ~45 nm, which is about the same dimension as with the cylindrical aggregate, $R_{g,cyl}$ (see Table 1). Apparently, the "mesh" is a result of the random packing of cylindrical aggregates in a (loose) three-dimensional (3-D) network; see also the cartoons in Fig. 5. It is worth noting, however, that the results gathered in Table S3, ESI† indicate that the value of ξ enlarges appreciably with increased gelation time, while the

This journal is © The Royal Society of Chemistry 2019

Published on 12 September 2019. Downloaded by National Synchrotron Radiation Research on 1/9/2020 4:42:14 AM.

Table 1 Material properties extracted from combined SALS/SLS/SAXS analysis for the Lw-pBTTT-C_{16}/CB sol at 15 °C

Methods	Parameters		Sol
SALS/SLS/SAXS	Microgel & cylinder bundle (eqn (S1), ESI)	$I_G(0)$ [a.u.]	5506
		Radius of gyration (R_g) [nm]	998
		$I_L(0)$ [a.u.]	880
		Characteristic length (ξ) [nm]	184
		Fractal dimension (d_f)	2.1
		Radius of gyration $R_{g,clust}$ $S(q)$ [nm] [a]	570
		Length of cylindrical aggregates (L) [nm]	155
		Diameter of cylindrical aggregates (d) [nm]	27
		Radius of gyration of cylindrical aggregates $R_{g,cyl}$ [nm] [b]	48.6
	Isolated gelator & cylinder interior (eqn (S3), ESI)	$I_P(0)$ [a.u.]	0.15
		Length (L) [nm]	14.9
		Diameter (d) [nm]	3.9
		Radius of gyration $R_{g,iso}$ [nm] [b]	5.1
		$I_D(0)$ [a.u.]	0.06
		Characteristic length (ξ_d) [nm]	0.1
		Radius of packing gelator (R) [nm]	1.0

[a] Calculated from the relation $R_{g_}S(q) = [d_f(d_f + 1)]^{0.5}\xi$. [b] Calculated from the relation $R_g^2 = L^2/12 + d^2/2$.

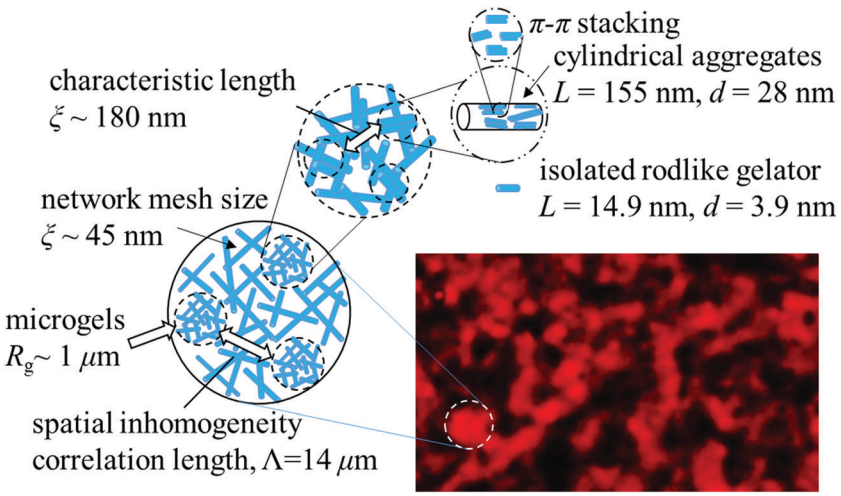

Fig. 5 Thin-film morphology taken from the OM image for the Lw-pBTTT-C_{16}/CB gel incubated at T = 15 °C and t = 24 h. The cartoons illustrate hierarchical structural features underlying the Lw-pBTTT-C_{16}/CB gel network. Note that at a later stage of gelation, some of the cylinders form semicrystalline bundles, not shown here.

$I(q) \sim q^{-2}$ behavior previously noticed at intermediate scales is gradually transformed into $I(q) \sim q^{-1}$ (see Fig. S12a, ESI†), suggesting that the cylinder bundles assume a more ordered and compact state. At sufficiently long gelation times (>10 h), the scattering intensity in this region eventually produces a pronounced peak at $q \sim 8.0 \times 10^{-2}$ nm^{-1}, as observed in Fig. 4b, indicative of the formation of ordered and compact (semicrystalline) cylinder bundles. At still longer gelation times, the peak sharpens and shifts toward higher q (Fig. S12b, ESI†), likely due to a further enhanced interaction between neighboring bundles.

In the highest-q (>0.1 nm^{-1}) region, the SAXS profile for both sol and gel reflects the contributions of the cylinder interior plus isolated gelators—the primary packing units of the former species. The existence of isolated gelators (*i.e.*, the first mode in the DLS analysis) is marked by some slight leveling that is followed by a further downturn at still higher q showing the behavior of $I(q) \sim q^{-4}$, indicative of the cross-sectional feature of a rod-like gelator. Thus, the SAXS profile for the Lw-pBTTT-C_{16}/CB sol may be described by eqn (S3) (Section S5, ESI†), which accounts for the cylinder interior structure (the 1st term[54–56]) and the geometrical feature of isolated (rod-like) gelators (the 2nd term). The model fits are shown by the dashed line in Fig. 4a superimposed on the SAXS data, with the material properties gathered in Table 1. According to the results gathered in Table 1, Fig. 5 pictorially summarizes the hierarchical structures underlying the Lw-pBTTT-C_{16}/CB gel in this study.

3.4 Local structural features of Lw-pBTTT-C_{16}/CB gel and drop-cast thin film

During the Lw-pBTTT-C_{16}/CB sol–gel transition, there is a notable red-shift in the absorption spectra (Fig. S1a, ESI†), although the characteristic peak at $q \sim 16$ nm^{-1} for (type-1) π–π stacking ($d \approx 3.7$ Å)[16,27,60] seems to be absent in the WAXS profile (Fig. S13a, ESI†) for the gelling sample. For comparison, the GIWAXS profiles shown in Fig. S13b and S14, ESI† for drop-cast thin films clearly reveal that both pBTTT-C_{16}/CB samples

Published on 12 September 2019. Downloaded by National Synchrotron Radiation Research on 1/9/2020 4:42:14 AM.

display highly textured semicrystalline domains with a similar *d*-spacing and pattern, while Lw-pBTTT-C_{16}/CB exhibits additionally a diffraction peak for (type-2) π–π stacking at 14.5 nm^{-1} ($d \approx 4.4$ Å), a poorer crystalline structure that is often associated with low-molecular-weight poly(3-hexyl)thiophene (P3HT) and lacks a pronounced shoulder peak in the UV-vis spectra as typically observed for its type-1 counterpart.[79,80] This major difference provides compelling evidence suggesting that the dominant effect of chain rigidity for the Lw-pBTTT-C_{16} molecule not only faciliates the formation of a rigid cylindrical aggregate in solution but it also promotes the local π–π stacking in thin film—albeit a less perfect type. A recent study, however, suggested that backbone rigidity that promotes intrachain charge transport could play a more important role in producing high-performance OTFTs than the regular π–π stacking that facilitates occasional interchain hopping.[81] Interestingly, the UV-vis absorption spectra presented in Fig. S15, ESI† reveal that Lw-pBTTT-C_{16} exhibits more red-shift than its Hw-pBTTT-C_{16} counterpart for the eventual gel state, while the drop-cast thin films exhibit little difference. It is important to note that, given the same chain ridigity, conjugated polymers typically exhibit more red-shift in solution as well as in thin film with increasing molecular weight due to an extended conjugation length. Thus, the above UV-vis features are clearly indicative of superior backbone rigidity for the Lw-pBTTT-C_{16} chains, especially in the gel state wherein the constituting chains mostly assume an extended chain conformation within assembled cylindrical aggregates, in contrast with the collapsed, coiled one for Hw-pBTTT-C_{16} chains within individual spherical aggregates. Moreover, the superiority in ac conductivity, as observed in Fig. 1, is likely due to the improved local (*via* enhanced backbone rigidity) and bulk (*via* highly overlapped cylinder bundles) electron transport for Lw-pBTTT-C_{16}.

3.5 Viscoelastic features of Lw-pBTTT-C_{16}/CB sol–gel transition

Fig. 6a shows that in the strain-sweep experiment, there exists a maximum for both G' and G'' of the Lw-pBTTT-C_{16}/CB gel before it eventually yields at still larger strains. According to the classification by Hyun *et al.*,[82] the above feature belongs to type-3 or "strong strain overshoot." In contrast, the Hw-pBTTT-C_{16}/CB gel under a similar condition exhibited solely a small maximum for G''[50] that has been classified as "weak strain overshoot." Moreover, the yield point occurs at a notably larger strain for the Lw-pBTTT-C_{16}/CB gel (*cf.*, 50 *vs.* 10%), while the magnitude of complex modulus (G^*) decreases by nearly a hundredfold. These combined features suggest that the Lw-pBTTT-C_{16}/CB gel is much softer and more resilient and, hence, can be processed more easily. Alternatively, the break point identified in the corresponding stress signal can be used to reveal the mechanical strength of a gel material that arises from supramolecular interactions.[51] As the maximal oscillatory stress preceding a notable stress reversal is treated as the break point, as shown in Fig. S16, ESI,† it is found that the Hw-pBTTT-C_{16}/CB gel (28.2 Pa) permits a considerably higher stress at break than the Lw-pBTTT-C_{16}/CB gel (3.1 Pa). This feature may be attributed to the fact that whereas the former utilizes colloidal bridging to form the gel, the latter involves primarily the overlap of cylinder bundles during gelation. Despite these disparities, the results of the frequency-sweep experiment shown in Fig. 6b–d are qualitatively very similar to those observed for the Hw-pBTTT-C_{16}/CB gelation.[50] Fig. S17, ESI† shows the time-dependent complex modulus (G^*) in the time-sweep experiment (with a strain amplitude of 0.01 and frequency of 10.0 rad s^{-1}) along with the Avrami plot, as described in detail in prior work.[50] The notably wavy feature of the dynamic modulus responses with increased gelation time was not observed with the Hw-pBTTT-C_{16}/CB gel, and similar phenomena have been reported for the gels formed by hydrogel composites,[83] bitumen/SBS/crystalline polymer,[84] and polybutadiene/polyisoprene blends.[85] A common feature shared by the diverse gel materials above appears to be the development of multiple microphase domains during the sol–gel transition, in contrast with the relatively uniform growth of gel network (as with Hw-pBTTT-C_{16}/CB) that produces no such wavy features. Overall, one sees that the kinetics of the sol–gel transition for the two pBTTT-C_{16}/CB samples can have a significant impact on the mechanical properties of their gels.

To summarize the central disparities in the gelation structure and mechanism between the two pBTTT-C_{16} samples in this study, the scheme shown in Fig. 7 puts further emphasis on the crucial stage of pristine solutions that foster wormlike *vs.* rod-like supramolecular conformations for pBTTT-C_{16} chains with varying backbone rigidity and, eventually, produce mesoscale aggregate species acting as distinct (spherical *vs.* cylindrical) packing units in the sol and gel stages.

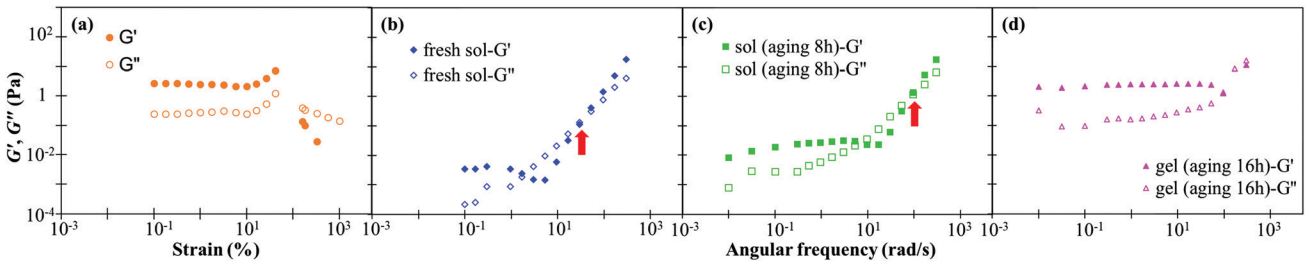

Fig. 6 Storage (G') and loss (G'') modulus responses for (a) strain sweep at an angular frequency of 10.0 rad s^{-1} for the gel incubated for 24 h at T = 15 °C, and frequency sweep at a strain of 0.01 for (b) t = 0, (c) t = 8, and (d) t = 16 h during the Lw-pBTTT-C_{16}/CB sol–gel transition at T = 15 °C. The arrows indicate the crossover points of G' and G'' in (b) and (c).

 This journal is © The Royal Society of Chemistry 2019

Published on 12 September 2019. Downloaded by National Synchrotron Radiation Research on 1/9/2020 4:42:14 AM.

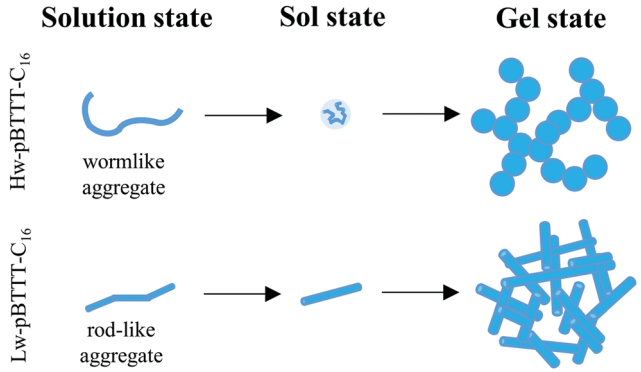

Fig. 7 Scheme grossly contrasting the gelation structure and mechanism of the two pBTTT-C_{16} samples in this study.

4. Conclusions

Lw-pBTTT-C_{16}/CB in this study is shown to form a gel at 15 °C through a distinct pathway of rod associations and networking when compared with its Hw-pBTTT-C_{16}/CB companion previously reported to capitalize on hierarchical colloidal bridging to form gels under identical experimental conditions. This major disparity in gelation kinetics is revealed to arise from the contrasting supramolecular conformations (rod-like *vs.* wormlike) of the aggregate clusters fostered in the pristine solution, leading to (mesoscale) cylindrical aggregates with a high persistence at 80 °C that do not collapse into spherical aggregates in the sol state at 15 °C as previously observed with Hw-pBTTT-C_{16}/CB. The ac conductivity measured at room temperature nearly doubles for Lw-pBTTT-C_{16}, attributable to the promoted local (*via* enhanced backbone rigidity) and bulk (*via* highly overlapped cylinder bundles) electron transport, while viscoelastic characterization also indicates that the Lw-pBTTT-C_{16} gel is much softer and more resilient, which, together, can greatly promote its processability. These combined features echo previous literature reports indicating that the molecular weight of the pBTTT-C_n series was among the essential factors that control both the morphological and electronic properties of the OTFTs fabricated, although the impact of polymer molecular weight is revealed herein to be indirectly acting through the supramolecular aggregate properties in solution. Clearly, the current findings and implications are of important concern invariably in future applications with the solution, sol, gel and thin film, and not limited to the sol–gel transition phenomenon and gel processability, for similar conjugated polymer species.

Conflicts of interest

There are no conflicts of interest to declare.

Acknowledgements

The authors thank the reviewers for constructive comments and suggestions. This research was supported by the Ministry of Science and Technology of ROC (MOST 107-2221-E-194-006). We acknowledge the NSRRC of ROC for providing beamtimes and facilitating the SAXS experiments.

References

1 A. Facchetti, *Chem. Mater.*, 2011, **23**, 733–758.
2 X. Guo, M. Baumgarten and K. Müllen, *Prog. Polym. Sci.*, 2013, **38**, 1832–1908.
3 T. A. Skotheim and J. Reynolds, *Conjugated Polymers: Theory, Synthesis, Properties, and Characterization*, CRC Press, Boca Raton, 2006.
4 Y. Liu, J. Zhao, Z. Li, C. Mu, W. Ma, H. Hu, K. Jiang, H. Lin, H. Ade and H. Yan, *Nat. Commun.*, 2014, **5**, 5293.
5 S. Günes, H. Neugebauer and N. S. Sariciftci, *Chem. Rev.*, 2007, **107**, 1324–1338.
6 R. D. Jansen-van Vuuren, A. Armin, A. K. Pandey, P. L. Burn and P. Meredith, *Adv. Mater.*, 2016, **28**, 4766–4802.
7 A. C. Grimsdale, K. Leok Chan, R. E. Martin, P. G. Jokisz and A. B. Holmes, *Chem. Rev.*, 2009, **109**, 897–1091.
8 H. Sirringhaus, *Adv. Mater.*, 2014, **26**, 1319–1335.
9 C. B. Nielsen, A. Giovannitti, D.-T. Sbircea, E. Bandiello, M. R. Niazi, D. A. Hanifi, M. Sessolo, A. Amassian, G. G. Malliaras, J. Rivnay and I. McCulloch, *J. Am. Chem. Soc.*, 2016, **138**, 10252–10259.
10 H.-J. Yen, C. Shan, L. Wang, P. Xu, M. Zhou and H.-L. Wang, *Polymers*, 2017, **9**, 25.
11 R. Hamilton, C. Bailey, W. Duffy, M. Heeney, M. Shkunov, D. Sparrowe, S. Tierney, I. McCulloch, R. J. Kline, D. M. DeLongchamp and M. Chabinyc, *Proc. SPIE*, 2006, **6336**, 633611.
12 L.-H. Zhao, R.-Q. Png, J.-M. Zhuo, L.-Y. Wong, J.-C. Tang, Y.-S. Su and L.-L. Chua, *Macromolecules*, 2011, **44**, 9692–9702.
13 A. Gasperini and K. Sivula, *Macromolecules*, 2013, **46**, 9349–9358.
14 J. Liu, I. A. Mikhaylov, J. Zou, I. Osaka, A. E. Masunov, R. D. McCullough and L. Zhai, *Polymer*, 2011, **52**, 2302–2309.
15 R. J. Kline, D. M. DeLongchamp, D. A. Fischer, E. K. Lin, L. J. Richter, M. L. Chabinyc, M. F. Toney, M. Heeney and I. McCulloch, *Macromolecules*, 2007, **40**, 7960–7965.
16 E. Cho, C. Risko, D. Kim, R. Gysel, N. Cates Miller, D. W. Breiby, M. D. McGehee, M. F. Toney, R. J. Kline and J.-L. Bredas, *J. Am. Chem. Soc.*, 2012, **134**, 6177–6190.
17 H. Wang, J. Liu and Y. Han, *Polymer*, 2013, **54**, 948–957.
18 H. Wang, J. Liu, Y. Xu and Y. Han, *J. Phys. Chem. B*, 2013, **117**, 5996–6006.
19 P.-S. Wang, H.-H. Lu, C.-Y. Liu and S.-A. Chen, *Macromolecules*, 2008, **41**, 6500–6504.
20 A. M. Gaikwad, Y. Khan, A. E. Ostfeld, S. Pandya, S. Abraham and A. C. Arias, *Org. Electron.*, 2016, **30**, 18–29.
21 D. Alberga, G. F. Mangiatordi, L. Torsi and G. Lattanzi, *J. Phys. Chem. C*, 2014, **118**, 8641–8655.
22 M. K. Singh, A. Kumar and R. Prakash, *Org. Electron.*, 2017, **50**, 138–146.
23 L. Chen, K. Zhao, X. Cao, J. Liu, X. Yu and Y. Han, *Polymer*, 2018, **149**, 23–29.

Published on 12 September 2019. Downloaded by National Synchrotron Radiation Research on 1/9/2020 4:42:14 AM.

24 M. J. Lee, D. Gupta, N. Zhao, M. Heeney, I. McCulloch and H. Sirringhaus, *Adv. Funct. Mater.*, 2011, **21**, 932–940.
25 D. M. DeLongchamp, R. J. Kline, Y. Jung, D. S. Germack, E. K. Lin, A. J. Moad, L. J. Richter, M. F. Toney, M. Heeney and I. McCulloch, *ACS Nano*, 2009, **3**, 780–787.
26 Q. Zhang, Y. Sun, F. Jiao, J. Zhang, W. Xu and D. Zhu, *Synth. Met.*, 2012, **162**, 788–793.
27 I. McCulloch, M. Heeney, C. Bailey, K. Genevicius, I. MacDonald, M. Shkunov, D. Sparrowe, S. Tierney, R. Wagner, W. Zhang, M. L. Chabinyc, R. J. Kline, M. D. McGehee and M. F. Toney, *Nat. Mater.*, 2006, **5**, 328–333.
28 S. S. Babu, V. K. Praveen and A. Ajayaghosh, *Chem. Rev.*, 2014, **114**, 1973–2129.
29 G. M. Newbloom, K. M. Weigandt and D. C. Pozzo, *Soft Matter*, 2012, **8**, 8854–8864.
30 G. M. Newbloom, K. M. Weigandt and D. C. Pozzo, *Macromolecules*, 2012, **45**, 3452–3462.
31 S. Malik, T. Jana and A. K. Nandi, *Macromolecules*, 2001, **34**, 275–282.
32 G. M. Newbloom, F. S. Kim, S. A. Jenekhe and D. C. Pozzo, *Macromolecules*, 2011, **44**, 3801–3809.
33 M. Koppe, C. J. Brabec, S. Heiml, A. Schausberger, W. Duffy, M. Heeney and I. McCulloch, *Macromolecules*, 2009, **42**, 4661–4666.
34 P. D. L. Iglesia and D. C. Pozzo, *Soft Matter*, 2013, **9**, 11214–11224.
35 M. J. Sobkowicz, R. L. Jones, R. J. Kline and D. M. DeLongchamp, *Macromolecules*, 2012, **45**, 1046–1055.
36 P.-T. Huang, Y.-S. Chang and C.-W. Chou, *J. Appl. Polym. Sci.*, 2011, **122**, 233–240.
37 B.-G. Kim, E. J. Jeong, H. J. Park, D. Bilby, L. J. Guo and J. Kim, *ACS Appl. Mater. Interfaces*, 2011, **3**, 674–680.
38 W. Xu, H. Tang, H. Lv, J. Li, X. Zhao, H. Li, N. Wang and X. Yang, *Soft Matter*, 2012, **8**, 726–733.
39 C.-Y. Chen, S.-H. Chan, J.-Y. Li, K.-H. Wu, H.-L. Chen, J.-H. Chen, W.-Y. Huang and S.-A. Chen, *Macromolecules*, 2010, **43**, 7305–7311.
40 Z.-Q. Lin, N.-E. Shi, Y.-B. Li, D. Qiu, L. Zhang, J.-Y. Lin, J.-F. Zhao, C. Wang, L.-H. Xie and W. Huang, *J. Phys. Chem. C*, 2011, **115**, 4418–4424.
41 C. C. Kitts and D. A. Vanden Bout, *Polymer*, 2007, **48**, 2322–2330.
42 M. Knaapila and A. P. Monkman, *Adv. Mater.*, 2013, **25**, 1090–1108.
43 J.-H. Chen, C.-S. Chang, Y.-X. Chang, C.-Y. Chen, H.-L. Chen and S.-A. Chen, *Macromolecules*, 2009, **42**, 1306–1314.
44 C.-Y. Chen, C.-S. Chang, S.-W. Huang, J.-H. Chen, H.-L. Chen, C.-I. Su and S.-A. Chen, *Macromolecules*, 2010, **43**, 4346–4354.
45 R. H. Guo, C. H. Hsu, C. C. Hua and S. A. Chen, *J. Phys. Chem. B*, 2015, **119**, 3320–3331.
46 J.-H. Chen, C.-W. Chiu, L.-C. Chen, S.-Y. Lai and C.-C. Lee, *Polymer*, 2012, **53**, 4843–4854.
47 D. Alcazar, F. Wang, T. M. Swager and E. L. Thomas, *Macromolecules*, 2008, **41**, 9863–9868.
48 S. Ludwigs, *P3HT Revisited-from Molecular Scale to Solar Cell Devices*, Springer, New York, 2015.
49 S. Malik and A. K. Nandi, *J. Appl. Polym. Sci.*, 2007, **103**, 2528–2537.
50 H.-L. Yi and C.-C. Hua, *Soft Matter*, 2018, **14**, 1270–1280.
51 S. Das, P. Chakraborty, A. Shit, S. Mondal and A. K. Nandi, *J. Mater. Chem. A*, 2016, **4**, 4194–4210.
52 P. Chakraborty, S. Das and A. K. Nandi, *Prog. Polym. Sci.*, 2019, **88**, 189–219.
53 S. Das, R. Ghosh, P. Routh, A. Shit, S. Mondal, A. Panja and A. K. Nandi, *ACS Appl. Nano Mater.*, 2018, **1**, 2306–2316.
54 M. H. Rahman, C.-Y. Chen, S.-C. Liao, H.-L. Chen, C.-S. Tsao, J.-H. Chen, J.-L. Liao, V. A. Ivanov and S.-A. Chen, *Macromolecules*, 2007, **40**, 6572–6578.
55 M. Knaapila, D. W. Bright, R. Stepanyan, M. Torkkeli, L. Almásy, R. Schweins, U. Vainio, E. Preis, F. Galbrecht, U. Scherf and A. P. Monkman, *Phys. Rev. E: Stat., Nonlinear, Soft Matter Phys.*, 2011, **83**, 051803.
56 M. Knaapila, R. Stepanyan, M. Torkkeli, V. M. Garamus, F. Galbrecht, B. S. Nehls, E. Preis, U. Scherf and A. P. Monkman, *Phys. Rev. E: Stat., Nonlinear, Soft Matter Phys.*, 2008, **77**, 051803.
57 B. H. Hamadani, D. J. Gundlach, I. McCulloch and M. Heeney, *Appl. Phys. Lett.*, 2007, **91**, 243512.
58 D. M. DeLongchamp, R. J. Kline, Y. Jung, E. K. Lin, D. A. Fischer, D. J. Gundlach, S. K. Cotts, A. J. Moad, L. J. Richter, M. F. Toney, M. Heeney and I. McCulloch, *Macromolecules*, 2008, **41**, 5709–5715.
59 D. M. DeLongchamp, R. J. Kline, E. K. Lin, D. A. Fischer, L. J. Richter, L. A. Lucas, M. Heeney, I. McCulloch and J. E. Northrup, *Adv. Mater.*, 2007, **19**, 833–837.
60 M. L. Chabinyc, M. F. Toney, R. J. Kline, I. McCulloch and M. Heeney, *J. Am. Chem. Soc.*, 2007, **129**, 3226–3237.
61 J. K. Lee, W. L. Ma, C. J. Brabec, J. Yuen, J. S. Moon, J. Y. Kim, K. Lee, G. C. Bazan and A. J. Heeger, *J. Am. Chem. Soc.*, 2008, **130**, 3619–3623.
62 C. V. Hoven, X.-D. Dang, R. C. Coffin, J. Peet, T.-Q. Nguyen and G. C. Bazan, *Adv. Mater.*, 2010, **22**, E63–E66.
63 J. A. Merlo and C. D. Frisbie, *J. Polym. Sci., Part B: Polym. Phys.*, 2003, **41**, 2674–2680.
64 Q. Sun, K. Park and L. Dai, *J. Phys. Chem. C*, 2009, **113**, 7892–7897.
65 H. L. Yi, C. H. Wu, C. I. Wang and C. C. Hua, *Macromolecules*, 2017, **50**, 5498–5509.
66 Y. H. Wen, P. C. Lin, C. C. Hua and S. A. Chen, *J. Phys. Chem. B*, 2011, **115**, 14369–14380.
67 M. D. Wehrman, S. Lindberg and K. M. Schultz, *J. Rheol.*, 2018, **62**, 437–446.
68 G. M. H. Wilkins, P. T. Spicer and M. J. Solomon, *Langmuir*, 2009, **25**, 8951–8959.
69 N. F. Mott, *J. Non-Cryst. Solids*, 1968, **1**, 1–17.
70 N. Mott, *Metal-Insulator Transitions*, Taylor & Francis, London, 1990.
71 J. Planès, A. Wolter, Y. Cheguettine, A. Proń, F. Genoud and M. Nechtschein, *Phys. Rev. B: Condens. Matter Mater. Phys.*, 1998, **58**, 7774–7785.
72 V. P. Arya, V. Prasad and P. S. A. Kumar, *J. Phys.: Condens. Matter*, 2012, **24**, 245602.

 This journal is © The Royal Society of Chemistry 2019

Published on 12 September 2019. Downloaded by National Synchrotron Radiation Research on 1/9/2020 4:42:14 AM.

73 J. Halim, E. J. Moon, P. Eklund, J. Rosen, M. W. Barsoum and T. Ouisse, *Phys. Rev. B*, 2018, **98**, 104202.
74 R. K. Layek, S. Samanta, D. P. Chatterjee and A. K. Nandi, *Polymer*, 2010, **51**, 5846–5856.
75 C. O. Yoon, M. Reghu, D. Moses, A. J. Heeger and Y. Cao, *Synth. Met.*, 1994, **63**, 47–52.
76 H.-L. Yi and C.-C. Hua, *Macromolecules*, 2019, **52**, 332–340.
77 M. Shibayama, T. Tanaka and C. C. Han, *J. Chem. Phys.*, 1992, **97**, 6829–6841.
78 M. Shibayama, H. Kurokawa, S. Nomura, M. Muthukumar, R. S. Stein and S. Roy, *Polymer*, 1992, **33**, 2883–2890.
79 A. Zen, M. Saphiannikova, D. Neher, J. Grenzer, S. Grigorian, U. Pietsch, U. Asawapirom, S. Janietz, U. Scherf, I. Lieberwirth and G. Wegner, *Macromolecules*, 2006, **39**, 2162–2171.
80 L. Li, J. Hollinger, A. A. Jahnke, S. Petrov and D. S. Seferos, *Chem. Sci.*, 2011, **2**, 2306–2310.
81 X. Zhang, H. Bronstein, A. J. Kronemeijer, J. Smith, Y. Kim, R. J. Kline, L. J. Richter, T. D. Anthopoulos, H. Sirringhaus, K. Song, M. Heeney, W. Zhang, I. McCulloch and D. M. DeLongchamp, *Nat. Commun.*, 2013, **4**, 2238.
82 K. Hyun, S. H. Kim, K. H. Ahn and S. J. Lee, *J. Non-Newtonian Fluid Mech.*, 2002, **107**, 51–65.
83 W. H. Marks, S. C. Yang, G. W. Dombi and S. K. Bhatia, *J. Long-Term Eff. Med. Implants*, 2012, **22**, 229–236.
84 T. Xia, L. Zhou, J. Xu, Y. Qin, W. Chen and J. Dai, *Constr. Build. Mater.*, 2018, **178**, 272–279.
85 R. Zhang, H. Cheng, C. Zhang, T. Sun, X. Dong and C. C. Han, *Macromolecules*, 2008, **41**, 6818–6829.